CdIn$_2$S$_4$/g-C$_3$N$_4$ heterojunction photocatalysts: enhanced photocatalytic performance and charge transfer mechanism

Di Li,[a] Fenfen Shi,[b] Deli Jiang,[b] Min Chen[b] and Weidong Shi*[b]

Heterojunction photocatalysts composed of CdIn$_2$S$_4$ (CIS) nanocrystals and graphitic carbon nitride (g-C$_3$N$_4$) nanosheets (CN) have been synthesized using a simple two-step wet chemistry method. In this system, CN nanosheets not only act as a substrate for the growth and uniform distribution of CIS nanocrystals but also play a key role in the photocatalytic degradation of organic pollutants with high efficiency. The CdIn$_2$S$_4$/g-C$_3$N$_4$ (CIS/CN) heterojunction photocatalysts exhibited better photocatalytic activity than that of pristine CIS and CN in photocatalytic degradation of both an organic dye (methyl orange) and an antibiotic (tetracycline hydrochloride). The enhanced photocatalytic performance might be ascribed to the formation of a heterojunction structure with strong interface interaction, which is beneficial to the photoinduced charge transfer between CIS and CN and efficient to accelerate the seperation of photogenerated electrons and holes. The as-synthesized heterojunction photocatalysts also showed good photocatalytic stability. After four cycles, the photocatalytic activity almost remains unchanged. The heterojunction photocatalysts with excellent photocatalytic performance and reusability may provide a new sight in the development of a photocatalyst with high efficiency for practical application of water purification.

Introduction

As the photocatalysis technology has attracted increasing attention in the field of energy, environment and materials in recent years, it is imperative to develop and prepare photocatalysts with excellent photocatalytic activity for practical applications.[1–3] Graphitic carbon nitride (g-C$_3$N$_4$), due to it is a prototypical two-dimensional (2D) nanosheet photocatalyst with suitable band gap (∼2.7 eV), large specific surface area and good chemical stability, has been considered as a promising photocatalytic material.[4–7] Though many works already have been focused on developing high performance g-C$_3$N$_4$ photocatalysts, due to its low light-harvesting ability, high inclination for recombination and slow interfacial kinetics for photocatalytic reaction, the solar-to-energy conversion efficiency of g-C$_3$N$_4$ photocatalyst is still far away from practical applications.[8–10]

To suppress the charge recombination and enhance the performance of g-C$_3$N$_4$, several ways can be attempted including variation of morphology, doping and constructing heterojunctions.[11–15] To date, the charge separation method that is widely used and focuses on the creation of a heterojunction structure by combining g-C$_3$N$_4$ with other semiconductors has attracted considerable attention because of its effectiveness in

photoinduced charge separation.[16–19] For example, Zhang *et al.* successfully constructed SnNb$_2$O$_6$ nanosheet/g-C$_3$N$_4$ nanosheet two-dimensional heterostructures. The optimum photocatalytic activity of SnNb$_2$O$_6$/g-C$_3$N$_4$ heterostructure is 30% for the degradation of organic pollution, which is about 3.9 times higher than that of pristine g-C$_3$N$_4$.[20] Shi *et al.* coupled NaNbO$_3$ nanowires with g-C$_3$N$_4$ to fabricate g-C$_3$N$_4$/NaNbO$_3$ nanowire heterojunction photocatalysts and due to the strong interface interaction between g-C$_3$N$_4$ and NaNbO$_3$, the as-synthesized photocatalyst improved over 8-fold higher activity than that of the pristine g-C$_3$N$_4$ for CH$_4$ production in visible-light-driven CO$_2$ reduction.[21] The strategies of this method are the transfer of electrons from the conduction band (CB) of semiconductor I with more negative position to the CB of the semiconductor II with less negative position and the migration of holes from the valence band (VB) of semiconductors II with more positive position to the VB of the semiconductors I with less positive position, which are resulted by the space-charge region at the interface and the induced electric field. This will endow the photocatalysts with better carrier separation efficiency, longer carrier lifetimes and enhanced photocatalytic reaction rates.

In this study, CdIn$_2$S$_4$/g-C$_3$N$_4$ heterojunction photocatalysts have been synthesized by a two-step wet chemistry method. The CdIn$_2$S$_4$ exhibited nanocrystal structure with a size less than 100 nm, the g-C$_3$N$_4$ showed a typical two-dimensional nanosheet shape, and the heterojunction photocatalysts have a close contact interface, which is beneficial to the charge transfer. A

[a] *Institute for Energy Research, Jiangsu University, Zhenjiang, Jiangsu, China, 212013*
[b] *School of Chemistry and Chemical Engineering, Jiangsu University, Zhenjiang, Jiangsu, China, 212013. E-mail: swd1978@ujs.edu.cn*

series of characterizations such as XPS spectra demonstrated the formation of heterojunction and the strong interface interaction between $CdIn_2S_4$ and $g-C_3N_4$. The as-prepared $CdIn_2S_4/g-C_3N_4$ heterojunction photocatalysts exhibited enhanced photocatalytic performance in the degradation of organic dye (MO) and antibiotic (TC). In addition, on the basis of the photocatalytic activity of photocatalysts, trapping experiment, and ESR spectra, the possible photocatalytic mechanism for the enhanced photocatalytic activity of the $CdIn_2S_4/g-C_3N_4$ was discussed in detail.

Experimental section

Synthesis of $CdIn_2S_4/g-C_3N_4$ heterojunction photocatalysts

$g-C_3N_4$ nanosheets were prepared according to the previously reported method.[22] The $CdIn_2S_4/g-C_3N_4$ heterojunction photocatalysts were synthesized by a hydrothermal method. In a typical experiment, 0.0277 g of $Cd(NO_3)_2 \cdot 4H_2O$ and 0.0878 g of $In(NO_3)_3 \cdot 4.5H_2O$ were added into 15 mL of distilled water, which contains 0.14 g of $g-C_3N_4$. Then, 16.3 mL of mercaptoacetic acid aqueous solution (0.2 mol L^{-1}) and 3.25 mL of aqueous solution of sodium sulfide (0.2 mol L^{-1}) were added into the abovementioned mixture. After stirring for another 1 h, the mixture was transferred into a Teflon-lined stainless steel autoclave (50 mL) and heated at 180 °C for 12 h, and then naturally cooled to room temperature. After washing several times with distilled water and ethanol, the as-obtained samples were dried in vacuum at 60 °C. The bare $CdIn_2S_4$ was synthesized by the same method without the addition of $g-C_3N_4$. The $g-C_3N_4$ sample is denoted as CN, $CdIn_2S_4$ is denoted as CIS, and $CdIn_2S_4/g-C_3N_4$ is denoted as CIS/CN.

Characterization

Transmission electron microscopy and high resolution transmission electron microscopy (TEM and HRTEM) images were taken on a Tecnai G2 F30 S-TWIN TEM instrument (FEI, America) with an accelerating voltage of 300 kV. Purity and crystallization of the products were characterized by powder X-ray diffraction on a D8 advance X-ray spectrometer (Bruker, Germany) with Cu-Kα radiation ($\lambda = 1.5406$ Å). X-ray photoelectron spectroscopy (XPS) was performed on an ADES 400 (VG, England) instrument with Mg K-ADES source. UV-vis diffuse reflectance spectra (DRS) were obtained on a Shimadzu UV-2401 spectrophotometer equipped with a spherical diffuse reflectance accessory. The electron spin resonance (ESR) signals of spin-trapped radicals were measured on a Bruker model ESR JES-FA200 spectrometer using spin-trap reagent DMPO in water and methanol. The photocurrent and electrochemical impedance spectroscopy (EIS) measurements were carried out in a conventional three-electrode, single-compartment quartz cell on an electrochemical station (CHI 660D).

Photocatalytic experiments

The photocatalytic activities of the CIS/CN were tested in the degradation reaction of methyl orange (MO, 10 mg L^{-1}) and tetracycline hydrochloride (TC, 10 mg L^{-1}) under irradiation of

a 500 W tungsten light lamp. For a typical photocatalytic experiment, 0.06 g of catalyst powder was added into 60 mL of the abovementioned MO solution in a quartz tube. Prior to the irradiation, the suspensions were magnetically stirred in the dark for 30 min to ensure the adsorption/desorption equilibrium. The abovementioned suspensions were kept under constant air-equilibrated conditions before and during the irradiation. At given time intervals (20 min or 30 min), about 4 mL of aliquots were sampled and centrifuged to remove the particles. The concentrations of MO and TC were monitored using a UV-vis spectrophotometer according to its absorbance at 464 nm and 356 nm, respectively.

Results and discussion

The morphology and microstructure of the as-prepared photocatalysts were characterized by TEM images. As shown in Fig. 1a, the bare CIS exhibits quasi-octahedron nanostructure with a unit size less than 100 nm. The CN shows a typical two-dimensional nanosheet morphology with an ultra-thin thickness. When the heterojunction formed by CIS and CN, the CIS nanocrystals distribute on the surface of the CN nanosheets and show the close contact, which could be seen in Fig. 1c and d. The HAADF-STEM image (Fig. 1e) also further confirms the abovementioned results. The HRTEM image of CIS/CN shows that the lattice spacing is 0.325 nm, corresponding to (311) plane of cubic phase CIS. Due to the weak crystallinity, there is no apparent lattice spacing of CN shows in the HRTEM image.
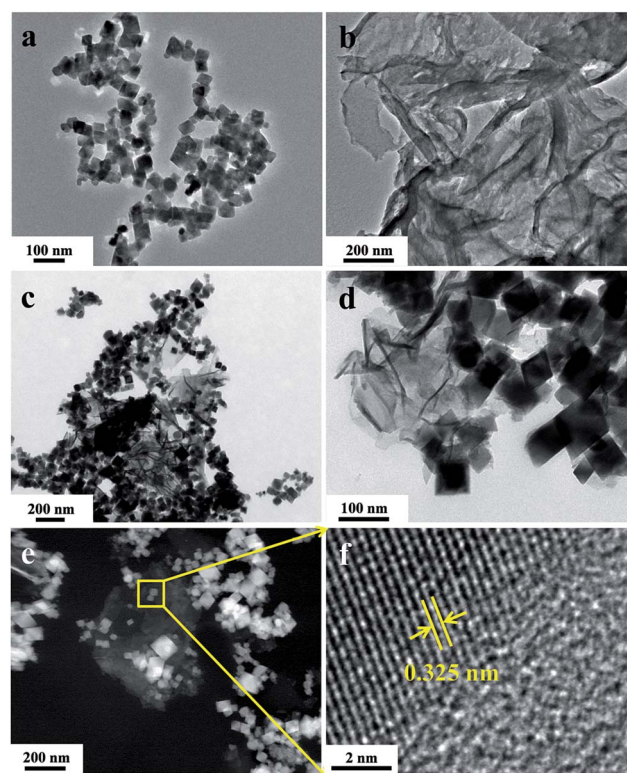

Fig. 1 TEM images of pristine CIS (a), CN (b) and CIS/CN (c and d), HAADF-STEM image (e) and HRTEM image (f) of CIS/CN.

In the XRD pattern (Fig. 2a) of CIS/CN, all the diffraction peaks can be assigned to both CN and CIS, and there are no other peaks can be detected, which indicate that no impurity has been produced during the formation of the heterojunction. The (100) and (002) peaks at 13.2° and 27.1° are originated from graphitic carbon nitride. The diffraction peaks of as-prepared CIS can be assigned to cubic $CdIn_2S_4$ (JCPDS no. 27-0060) with lattice constants of $a = 10.845$ nm, and the 14.0°, 23.2°, 27.3°, 33.0°, 40.8°, 43.4°, 47.4°, 55.7°, and 66.2° can be indexed to the (111), (220), (311), (400), (422), (511), (440), (533) and (731) planes, respectively. In the CIS/CN, an obvious (002) diffraction peak of CN appeared along with the standard peaks of pristine CIS, demonstrating that the CIS/CN is a mixture of CIS and CN. No other diffraction peaks were detected, which indicates that no impurity phase has been generated during the hydrothermal process.

The surface chemical composition of CIS, CN and CIS/CN was investigated by XPS analysis. Fig. 2b shows the XPS survey spectra of CIS, CN and CIS/CN. C, N, Cd, In and S can be detected in the XPS survey spectrum of CIS/CN. No other signal can be detected in the XPS spectrum of CIS/CN, implying that no impurity has been generated during the composite process.

Fig. 2c exhibits the high-resolution XPS spectra of Cd 3d of CIS/CN and CIS. As exhibited in Fig. 2c, peaks at 404.6 and 411.3 eV of CIS/CN are attributed to Cd $3d_{5/2}$ and Cd $3d_{3/2}$,[23] respectively, which shift slightly (~0.4 eV) to the lower binding

energy than the XPS peaks of CIS. Fig. 2d is the high-resolution XPS spectra of C 1s of CIS/CN and CN. The peaks at 284.6 eV of CIS/CN can be assigned to C–C graphite-like sp^2 structure and 288.5 eV is attributed to N–sp^3 C bond.[24,25] Due to the strong electronic interaction between CIS and CN, the Cd 3d peaks of CIS/CN shift toward a lower binding energy region. Furthermore, the binding energy of N–sp^3 C bond shifts about 0.3 eV to the higher binding energy than the XPS peaks of CN; however, the peak at 284.6 eV almost does not change, which indicates that the effect of CRef. 15: Please provide the last name for the 4th author.C bond on the interfacial interaction is less than the effect of C–N bond. These results imply that the CIS/CN is a heterojunction structure rather than a physical mixture of two pure phases of CIS and CN.[26]

As shown in the UV-vis spectra (Fig. 2e), the absorption band of CIS/CN is similar to the pure CIS, except that the absorption edge of CIS/CN shifts to the area of UV light, which might be caused by the addition of CN with poor visible light absorption ability. To investigate the band gap of CIS/CN, we calculated the band gap of CIS and CN using the Kubelka–Munk equation,[27] and the plot of $(\alpha h\nu)^x$ vs. $h\nu$ ($x = 1/2$ or 2) for the band gap energy of CIS and CN is shown in Fig. 2f. Due to the direct gap nature of CIS and indirect gap nature of CN, the band gap of CIS and CN is approximately 2.3 eV and 2.7 eV, respectively. Both the band gap values of CIS and CN are close to previous literature reports.[4,28]

To investigate the photocatalytic activity of the as-prepared CIS/CN heterojunction photocatalyst, MO was used as a target organic pollutant, and photocatalytic degradation of MO under visible-light has been employed in this study. The MO exhibited very low degradation rate and reaction rate constant k under the visible-light irradiation in the absence of a photocatalyst in the photocatalytic system indicating the relative photostability of MO (Fig. 3a and b). As shown in Fig. 3a, after 100 min of photocatalytic reaction, the degradation rate of pure CIS and CN is 52% and 37%, respectively. However, the degradation rate of CIS/CN is much higher than both CIS and CN, and the value is 91%, which suggests that the CIS/CN exhibits better photocatalytic performance than CIS and CN. All of these data have excluded the effect of MO absorption on the surface of the photocatalysts. Fig. 3b shows the kinetic fit and degradation rate constant k for the degradation of MO with CIS, CN, CIS/CN and blank. All plots of $\ln(C_0/C)$ against reaction time exhibit a linear relationship, indicating that the MO photocatalytic degradation was described well with the pseudo-first-order model.[29] The reaction rate constant k of CIS, CN and CIS/CN is 0.00737, 0.00448 and 0.02349, and the k of CIS/CN is about 3.19 times and 5.24 times higher than pure CIS and CN, respectively.

We also studied the photocatalytic stability of CIS/CN in the degradation of MO, and the results are shown in Fig. 3c and d. As shown in Fig. 3c, after four recycles, the activity of photocatalytic degradation of MO remains relatively good, and only about 10% decline is observed than the first time. The XRD pattern of the used photocatalyst has almost no change, as shown in Fig. 3d. Both of these indicate that CIS/CN has superior stability during photocatalytic degradation of MO, and this is quite important in the practical application of a photocatalyst.
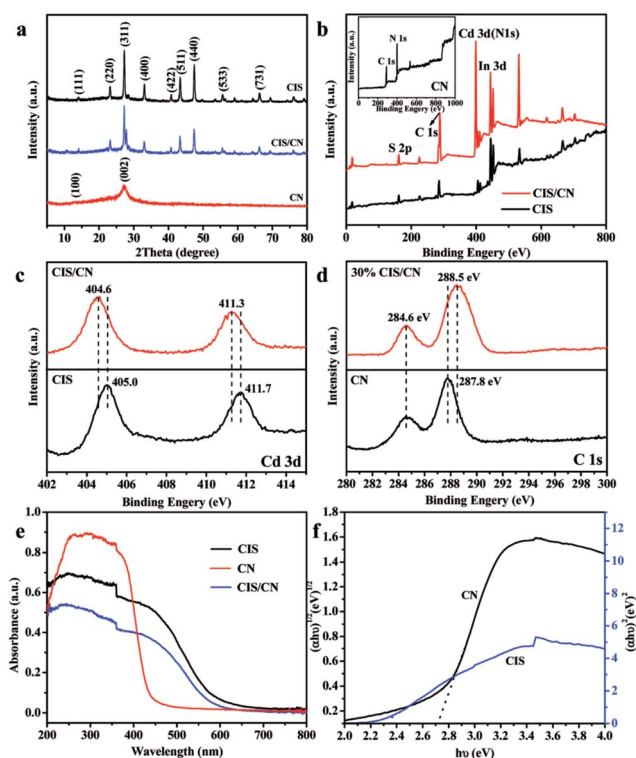

Fig. 2 (a) XRD patterns, (b) XPS survey spectra of CIS, CN (inset) and CIS/CN, (c and d) high-resolution XPS spectra of Cd 3d and C 1s, respectively, (e) UV-vis spectroscopy, and (f) plot of $(\alpha h\nu)^{1/2}$ vs. $h\nu$ for the band gap energy of CN and plot of $(\alpha h\nu)^2$ vs. $h\nu$ for the band gap energy of CIS.
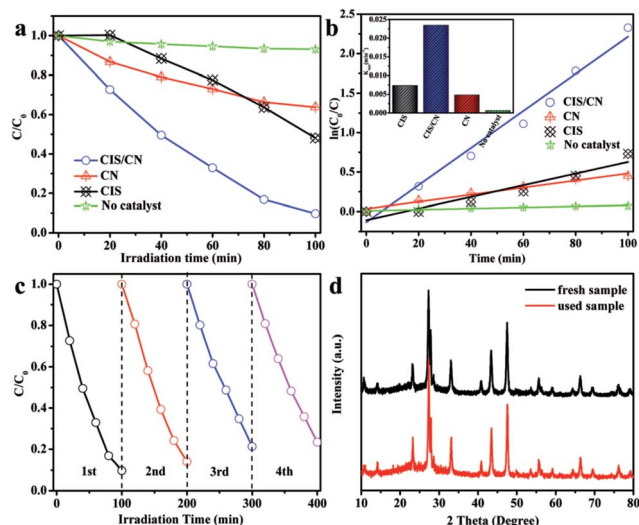
Fig. 3 (a) Photocatalytic degradation of MO and (b) kinetic fit and degradation rate constant k (inset in b) for the degradation of MO using CIS, CN, CIS/CN and in absence of photocatalyst, (c) cycling runs for the photodegradation of MO with CIS/CN, and (d) XRD patterns of the freshly prepared and used CIS/CN after four times cycling.

To further explore the photocatalytic performance of the as-prepared photocatalyst in degradation of other pollution, TC, as a typical antibiotic has been selected in our study. Fig. 4a shows the photocatalytic degradation curves. The CIS/CN shows the
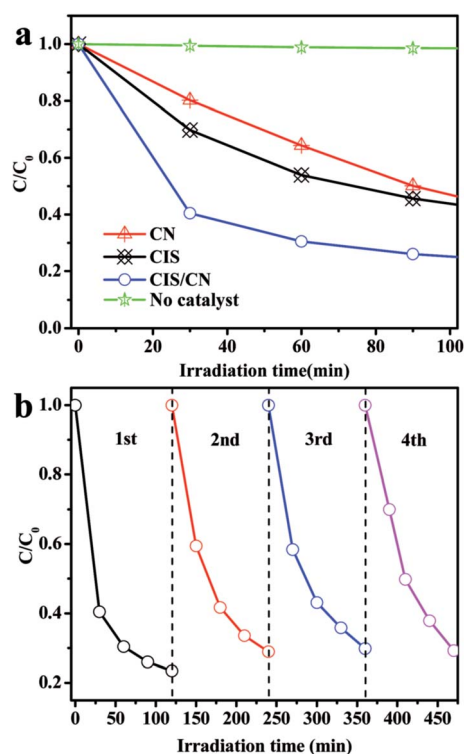

Fig. 4 (a) Photocatalytic degradation of TC in the presence of CIS, CN, CIS/CN and in the absence of photocatalyst and (b) cycling runs for the photodegradation of TC with CIS/CN.

best photocatalytic activity in the entire photocatalysis process. When there is no photocatalyst in the photocatalysis reaction, a very low TC degradation was observed under visible-light irradiation, indicating that the TC is photochemically resistant. On adding the photocatalyst into the photocatalytic reaction, in the first 30 min, the degradation rate of CIS/CN reached 60%, whereas the degradation rates of CIS and CN are 30% and 20%, respectively. When the photocatalytic reaction time reaches 120 min, the degradation rate of CIS/CN is nearly 80% and the degradation rates of CIS and CN are about 60%. The better photocatalytic activity of CIS/CN might be due to the formation of heterojunction. The photocatalytic stability of CIS/CN in the degradation of TC also has been discussed in our study. As illustrated in the cycling runs curves (Fig. 4b), the CIS/CN heterojunction photocatalyst also exhibits excellent photocatalytic stability.

To deeply discuss the reaction mechanism, the main active species in the degradation process has been investigated by the trapping experiment, in which ammonium oxalate (AO) was used as the hole (h^+) scavenger, 1,4-benzoquinone (BQ) was used as the $\cdot O_2^-$ scavenger, and *tert*-butanol (TBA) was used as the hydroxyl radical ($\cdot OH$) scavenger.[30] As shown in Fig. 5a, when TBA was added in the reaction, the photocatalytic degradation rate shows very little decrease, which indicates that $\cdot OH$ plays a minor role in degradation of organic pollutants. In comparison, the photocatalytic activity of CIS/CN decreased apparently by the addition of AO and BQ, which suggests that h^+ and $\cdot O_2^-$ act as main oxidative species in the process of photocatalytic degradation of organic pollution. Furthermore, when O_2 is limited in the photocatalytic reaction, a great reduction of photocatalytic activity has been observed, which proves that O_2 primarily acts as the efficient electron trap and results in the generation of $\cdot O_2^-$.

For further confirmation of the abovementioned results, DMPO spin-trapping ESR technique has been adopted. As exhibited in Fig. 5b, the ESR signal intensities recorded with CIS/CN in an aqueous dispersion are almost the same as in the dark when the light is on, which suggests that there is little $\cdot OH$ generated in this system, and $\cdot OH$ is not the main reactive species. However, when the ESR signal intensities recorded with CIS/CN in methanol dispersion with the light on, the characteristic peaks of DMPO-$\cdot O_2^-$ can be clearly detected and are quite sharper than in the dark condition. Thus, it is well recognized that $\cdot O_2^-$ can be generated in this system and played an important role in the photocatalytic degradation of organic pollutants, which are well consistent with the results of the trapping experiment.[31]

To understand the mechanism of photogenerated charge transfer in a CIS/CN heterojunction photocatalyst under visible-light irradiation, we first studied the specific surface area of CIS, CN and CIS/CN photocatalysts. Fig. 6 shows the adsorption–desorption isotherms from the adsorption branches. The N_2 adsorption–desorption isotherm for all the photocatalyst samples is identified as a type IV isotherm with a H1 hysteresis loop according to Brunauer–Deming–Deming–Teller (BDDT) classification.[32] The BET surface areas of CIS, CN and CIS/CN are 36.9 cm³ g⁻¹, 36.6 cm³ g⁻¹ and 30.5 cm³ g⁻¹, respectively.
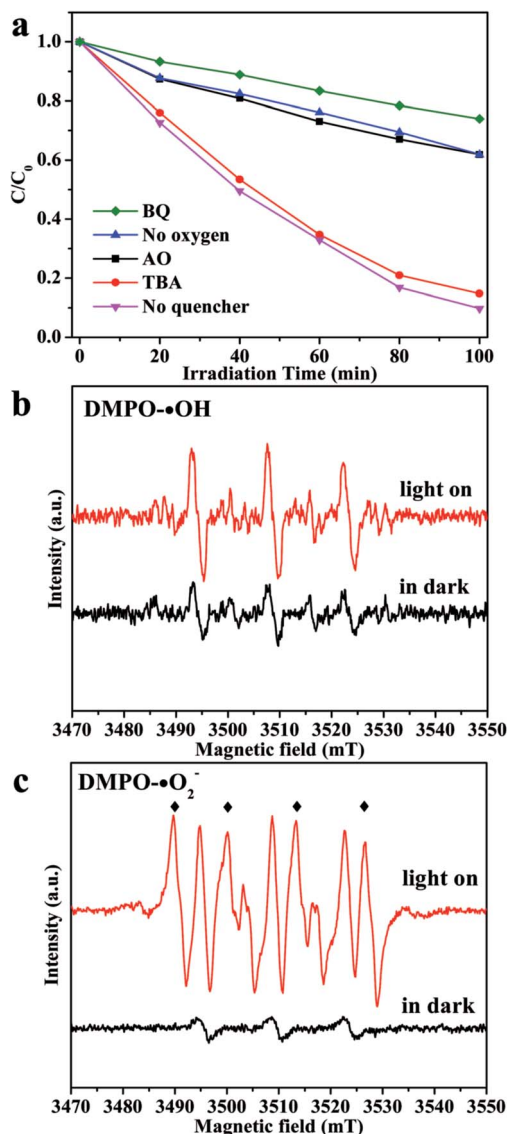
Fig. 5 (a) Trapping experiment of active species during the photocatalytic degradation of MO using CIS/CN under visible-light, and DMPO spin-trapping ESR spectra recorded with CIS/CN in aqueous dispersion for DMPO-$\cdot$OH (b) and in methanol dispersion for DMPO-$\cdot$O$_2^-$ (c).

The BET surface area of CIS/CN is smaller than both of CIS and CN, the reason might be that when the CIS and CN hybridize together, a part of the porous structure was blocked by the contact of CIS and CN. Thus, the effect of the specific surface area can be excluded for the enhanced photocatalytic activity of CIS/CN.

The band edge position of the photocatalyst valence band (E_{VB}) and conduction band (E_{CB}) is quite important in the discussion of a photogenerated charge transfer route. The E_{VB} of the CIS can be calculated by the following equation:[33]

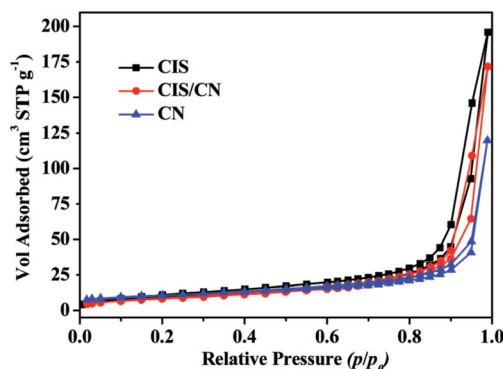$$E_{CB} = \chi - E^e - 0.5E_g$$

$$E_{VB} = E_{CB} - E_g$$

Fig. 6 Adsorption–desorption isotherms from the adsorption branches of CIS, CN and CIS/CN.

where χ is the electronegativity of the semiconductor, E^e is energy of free electrons on the hydrogen scale ($\sim$4.5 eV). Based on the equation, the E_{CB} and E_{VB} of CIS are determined at -0.81 eV and 1.5 eV, and the E_{CB} and E_{VB} of CN are determined at -1.3 eV and 1.4 eV, respectively.

On the basis of the abovementioned characterizations and results, a possible mechanism of charge transfer in CIS/CN is proposed. As shown in Fig. 7, because of the existence of an interface between CIS and CN, the electrons generated from CB of CN with more negative CB edge potential will transfer to the conduction band of CIS under the visible-light irradiation. Because the energies of CB edge of CIS is more negative than the standard redox potential $E^{\ominus}(O_2/\cdot O_2^-)$ (-0.33 V $vs.$ NHE),[34] O$_2$ existing in the photocatalytic system can be reduced to $\cdot$O$_2^-$. Then, $\cdot$O$_2^-$ can act as an active species in the photocatalytic degradation of the organic pollutants to CO$_2$, H$_2$O and other small molecules. Moreover, the holes excited from the VB of CIS with more positive VB edge potential will flow to the VB of CN. Due to the strong oxidizing nature of the photogenerated holes, part of the holes could also play an important role in the photocatalytic degradation of organic pollutants. The photocatalysis process of CIS/CN photocatalyst accord with the photocatalysis process of a typical type II heterojunction structure, which is beneficial for the photogenerated charge transfer and efficient to suppress the recombination of electrons and holes.
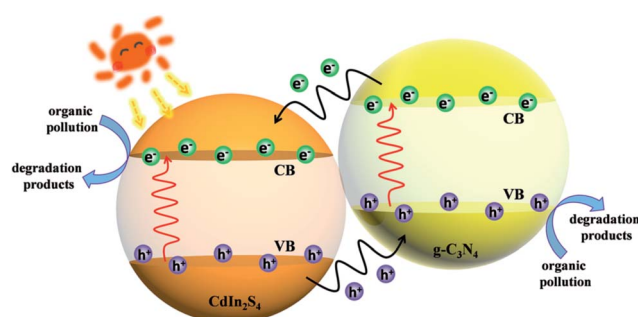

Fig. 7 Possible mechanism of charge transfer in a CIS/CN heterojunction photocatalyst under visible-light irradiation.
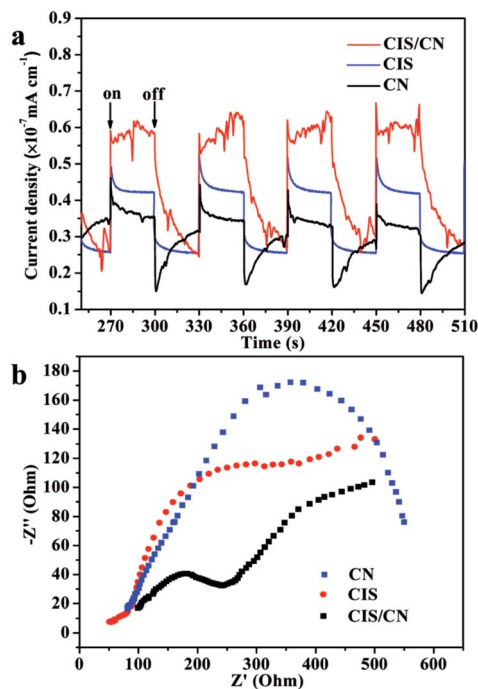
Fig. 8 (a) Transient photocurrent responses and (b) EIS Nyquist plots of CIS, CN and CIS/CN.

In order to support the abovementioned mechanism, the relative charge recombination efficiency of CIS, CN and CIS/CN has been studied using transient photocurrent responses and Nyquist plot of EIS. As shown in Fig. 8a, after four on–off cycles, the generation of photocurrent exhibits good reproducibility with stable photocurrent intensity for all samples. It can be known from the data that the photocurrent of the CIS/CN electrode is about 2.1 times and 1.7 times higher than that of CIS and CN electrodes, respectively, which indicates that an enhanced photoinduced electrons and holes separation could be caused by the formation of heterojunction structure. These results also could be confirmed by the Nyquist plots of EIS. Owing to the radius of the arc on the EIS Nyquist plot reports the charge transfer rate occurring at the contact interface between the working electrode and electrolyte solution, the smaller arc radius suggests the higher efficiency of photoinduced charge transfer.[35] As shown in Fig. 8b, CIS/CN exhibits the smaller radius of arc, which demonstrates that the heterojunction structure is beneficial to improve the charge transfer efficiency. Both transient photocurrent responses and EIS Nyquist plots can further account for the better photocatalytic performance of CIS/CN and confirm the possible mechanism of charge transfer in CIS/CN.

Conclusions

In summary, heterojunction photocatalysts composed of CIS nanocrystals and CN nanosheets have been prepared *via* a two-steps wet chemistry approach. The formation of a heterojunction structure and strong interface interaction between CIS and CN were characterized by XPS spectra, and they could

efficiently enhance the photogenerated charge transfer and suppress the recombination of electrons and holes, which also have been demonstrated by the transient photocurrent responses and Nyquist plots of EIS. The as-prepared photocatalysts exhibited enhanced photocatalytic activity than pristine CIS and CN. The reaction rate constant k in photocatalytic degradation of MO is about 3.19 times and 5.24 times higher than pure CIS and CN, respectively. The CIS/CN also showed excellent photocatalytic performance in degradation of TC. Moreover, the CIS/CN heterojunction photocatalysts exhibited good photocatalytic stability and reusability, which are very important index for the practical application of photocatalyst.

Acknowledgements

Notes and references

1 J. Z. Chen, X. J. Wu, L. S. Yin, B. Li, X. Hong, Z. X. Fan, B. Chen, C. Xue and H. Zhang, *Angew. Chem., Int. Ed.*, 2014, **53**, 1–6.

2 L. D. Li, J. Q. Yan, T. Wang, Z. J. Zhao, J. Zhang, J. L. Gong and N. J. Guan, *Nat. Commun.*, 2015, **6**, 5881.

3 C. Han, Z. Chen, N. Zhang, J. C. Colmenares and Y. J. Xu, *Adv. Funct. Mater.*, 2015, **25**, 221–229.

4 X. C. Wang, K. Maeda, A. Thomas, K. Takanabe, G. Xin, J. M. Carlsson, K. Domen and M. Antonietti, *Nat. Mater.*, 2009, **8**, 76–80.

5 X. H. Li, J. S. Chen, X. C. Wang, J. H. Sun and M. Antonietti, *J. Am. Chem. Soc.*, 2011, **133**, 8074–8077.

6 W. J. Ong, L. L. Tan, Y. H. Ng, S. T. Yong and S. P. Chai, *Chem. Rev.*, 2016, **116**, 7159–7329.

7 H. J. Yu, L. Shang, T. Bian, R. Shi, G. I. N. Waterhouse, Y. F. Zhao, C. Zhou, L. Z. Wu, C. H. Tung and T. R. Zhang, *Adv. Mater.*, 2016, **28**, 5080–5086.

8 F. Dong, Z. W. Zhao, Y. J. Sun, Y. X. Zhang, S. Yan and Z. B. Wu, *Environ. Sci. Technol.*, 2015, **49**, 12432–12440.

9 D. L. Jiang, J. Li, C. S. Xing, Z. Y. Zhang, S. C. Meng and M. Chen, *ACS Appl. Mater. Interfaces*, 2015, **7**, 19234–19242.

10 Y. F. Li, R. X. Jin, Y. Xing, J. Q. Li, S. Y. Song, X. C. Liu, M. Li and R. C. Jin, *Adv. Energy Mater.*, 2016, 1601273.

11 X. F. Yang, Z. P. Chen, J. S. Xu, H. Tang, K. M. Chen and Y. Jiang, *ACS Appl. Mater. Interfaces*, 2015, **7**, 15285–15293.

12 J. Ran, T. Y. Ma, G. Gao, X. W. Du and S. Z. Qiao, *Energy Environ. Sci.*, 2015, **8**, 3708–3717.

13 H. J. Kong, H. W. Da, J. Kim and S. I. Woo, *Chem. Mater.*, 2016, **28**, 1318–1324.

14 D. L. Jiang, T. Y. Wang, Q. Xu, D. Li, S. C. Meng and M. Chen, *Appl. Catal., B*, 2017, **201**, 617–628.

15 R. R. Hao, G. H. Wang, H. Tang, L. L. Sun, C. Xu and D. Y. Han, *Appl. Catal., B*, 2016, **187**, 47–58.

16 F. T. Lia, Y. Zhao, Q. Wang, X. J. Wang, Y. J. Hao, R. H. Liu and D. S. Zhao, *J. Hazard. Mater.*, 2015, **283**, 371–381.

17 F. T. Li, S. J. Liu, Y. B. Xue, X. J. Wang, Y. J. Hao, J. Zhao, R. H. Liu and D. S. Zhao, *Chem.–Eur. J.*, 2015, **21**, 10149–10159.

18 X. J. Wang, Q. Wang, F. T. Li, W. Y. Yang, Y. Zhao, Y. J. Hao and S. J. Liu, *Chem. Eng. J.*, 2013, **234**, 361–371.

19 X. J. Wang, W. Y. Yang, F. T. Li, Y. B. Xue, R. H. Liu and Y. J. Hao, *Ind. Eng. Chem. Res.*, 2013, **52**, 17140–17150.

20 Z. Y. Zhang, D. L. Jiang, D. Li, M. Q. He and M. Chen, *Appl. Catal., B*, 2016, **183**, 113–123.

21 H. F. Shi, G. Q. Chen, C. L. Zhang and Z. G. Zou, *ACS Catal.*, 2014, **4**, 3637–3643.

22 D. L. Jiang, L. L. Chen, J. M. Xie and M. Chen, *Dalton Trans.*, 2014, **43**, 4878–4885.

23 H. Liu, Z. Z. Xu, Z. Zhang and D. Ao, *Appl. Catal., A*, 2016, **518**, 150–157.

24 Y. S. Xu and W. D. Zhang, *ChemCatChem*, 2013, **5**, 2343–2351.

25 C. C. Han, L. Ge, C. F. Chen, Y. J. Li, X. L. Xiao, Y. N. Zhang and L. L. Guo, *Appl. Catal., B*, 2014, **147**, 546–553.

26 Y. L. Tian, B. B. Chang, J. L. Lu, J. Fu, F. N. Xi and X. P. Dong, *ACS Appl. Mater. Interfaces*, 2013, **5**, 7079–7085.

27 D. Li, X. C. Duan, Q. Qin, H. M. Fan and W. J. Zheng, *J. Mater. Chem. A*, 2013, **1**, 12417–12421.

28 B. B. Kale, J. O. Baeg, S. M. Lee, H. Chang, S. J. Moon and C. W. Lee, *Adv. Funct. Mater.*, 2006, **16**, 1349–1354.

29 D. Li, W. D. Shi and W. J. Zheng, *J. Cryst. Growth*, 2016, **448**, 93–96.

30 Y. H. Ao, K. D. Wang, P. F. Wang, C. Wang and J. Hou, *Appl. Catal., B*, 2016, **194**, 157–168.

31 S. Q. Guo, M. M. Zhen, M. Q. Sun, X. Zhang, Y. P. Zhao and L. Liu, *RSC Adv.*, 2015, **5**, 16376–16385.

32 D. Li, Q. Qin, X. C. Duan, J. Q. Yang, W. Guo and W. J. Zheng, *ACS Appl. Mater. Interfaces*, 2013, **5**, 9095–9100.

33 N. Liang, J. T. Zai, M. Xu, Q. Zhu, X. Wei and X. F. Qian, *J. Mater. Chem. A*, 2014, **2**, 4208–4216.

34 X. L. Fu, W. M. Tang, L. Ji and S. F. Chen, *Chem. Eng. J.*, 2012, **180**, 170–177.

35 D. M. Chen, K. W. Wang, D. G. Xiang, R. L. Zong, W. Q. Yao and Y. F. Zhu, *Appl. Catal., B*, 2014, **147**, 554–561.